Monitoring Cobalt-Oxide Single Particle Electrochemistry with sub-Diffraction Accuracy

Vitor Brasiliense,[a] Jan Clausmeyer,[b] Pascal Berto,[c] Gilles Tessier,[c] Catherine Combellas,[a] Wolfgang Schuhmann,[b] Fréderic Kanoufi[a,*]

[a] Université Sorbonne Paris Cité, Université Paris Diderot, ITODYS, CNRS UMR 7086, 15 rue Jean-Antoine de Baïf, F-75013 Paris, France.
[b] Analytical Chemistry - Center for Electrochemical Sciences (CES), Ruhr-Universität Bochum, Universitätsstraße 150, D-44780 Bochum, Germany
[c] Université Sorbonne Paris Cité, Université Paris Descartes, Neurophotonics Laboratory, CNRS UMR 8250, 45 Rue des Saints Pères, F-75006 Paris, France

ABSTRACT: By partially overcoming the diffraction limit, super-localization techniques have extended the applicability of optical techniques down to the nanometer size-range. Herein, cobalt oxide-based nanoparticles are electrochemically grown onto carbon nanoelectrodes and their individual catalytic properties are evaluated through a combined electrochemical-optical approach. Using dark-field white light illumination, edges super-localization techniques are applied to quantify changes in particle size during electrochemical activation with down to 20nm precision. It allows the monitoring of (i) the anodic electrodeposition of cobalt hydroxide material and (ii) the large and reversible volume expansion experienced by the cobalt hydroxide particle during its oxidation. Meanwhile, the particle light scattering provides chemical information such as the Co redox state transformation, which complements both the particle size and the recorded electrochemical current and provides *in operando* mechanistic information on particle electrocatalytic properties.

Efficient heterogeneous catalysis is a long-sought milestone on the way towards cleaner sources of energy. In this context, electrochemical water splitting to generate hydrogen fuel has drawn much attention lately owing to the possibility of being coupled to solar energy. Particularly, cobalt-oxide-based materials have received special attention over the past years[1] due to their ability to perform highly efficient long-term catalysis of the oxygen evolution reaction (OER) and to their self-healing capability.[2] If pure electrochemical approaches based on the careful reading of voltammograms[3,4] can unravel the redox and chemical aspects of the catalytic reactivity of these systems, their correlation, under operating conditions, to *in situ* structural complementary observations such as SEM,[2] STM[5-7] or X-ray spectroscopies is a real asset.[5-10] This is mainly performed on thin layers; however, the electrodeposition of cobalt-oxide-based materials through Co^{2+} oxidation leads to films nucleated from globular particles with characteristic sizes ranging from a few tens of nanometers to micrometers.[11-13] Since the size and morphology of transition metal catalysts,[14,15] such as cobalt,[16] may drastically affect their activities, the coupling of *in operando* complementary monitoring to single nanoparticle electrochemistry is particularly promising.

Recent developments in electroanalysis allow interrogating electrocatalytic reaction mechanisms at the single nanoparticle level,[17-20] from purely electrochemical strategies such as electrochemical nanoimpacts,[21] by using nanosized electrochemical cells,[22,23] from the controlled deposition of the nanoobject on a nanoelectrode,[15,24-27] or from their imaging by scanning electrochemical nanoprobes.[28-30]

Electromagnetic waves (e. g. visible-light, X-ray) microscopies can allow fast full-field imaging. Electron microscopies and nano X-ray techniques[31,32] provide the highest resolution *in situ* imaging of nanoparticle electrochemistry, although their radiations can induce chemical side effects.[33] Several groups, including ours, are suggesting that super-localization optical microscopies[34-41] are easier to implement to image electrochemical processes at individual nanoobjects in the 20-100 nm range, in two or three dimensions, with high temporal resolution and negligible material damage. The super-localization capacity of these microscopies has already been used, mainly, to track the position of single particle,[34-41] while complementary chemical information was extracted from the recorded optical signature of the particle.[34,35,37-40] These optical microscopies have mainly addressed the electrochemistry of individual plasmonic particles, such as noble metals[35,37] or recently Co-oxides to monitor (i) their formation during cathodic Co electrodeposition,[38] or (ii) Li^+ ion insertion during battery cyclability.[34]

Herein, we propose to use the super-localization strategy to monitor with sub-100nm resolution the variation of particle size while it is actuated electrochemically. This *in operando* optical nanoscopy approach is illustrated in the electrochemistry of a single cobalt-oxide particle during its growth and during electrocatalytic performance, but can also be applied to various systems showing deformation. Here, a carbon nanoe-

lectrode scaffold is used as a unique means to grow, support and electrochemically interrogate[15,25,38] single cobalt-oxide particles of sizes in the 0.5-3µm range. These particles are comparable to the ensembles of particles usually studied in films,[11-13,42] with the added advantage of keeping the particle under study in a fixed position, at the apex of the nanoelectrode. Single particle electrochemistry is complemented by the optical monitoring of size variations through super-localization of particle edges and light scattering intensity. We first present how to adapt the superlocalization strategies to assess particle size accurately. Three examples related to Co-oxide electrochemistry of increasing complexity are used to case proof the proposed approach. In particular, the oxidation of Co-oxide is accompanied by a strong (reversible) volume expansion, which is quantitatively interpreted. When Co^{2+} is present in solution a further Co-oxide electroprecipitation growth is demonstrated. Since the optical response of the particle carries quantitative mechanistic information related to the change in redox state of the catalytically active Co species, we finally use the technique to gain further insight into electrocatalytic OER.

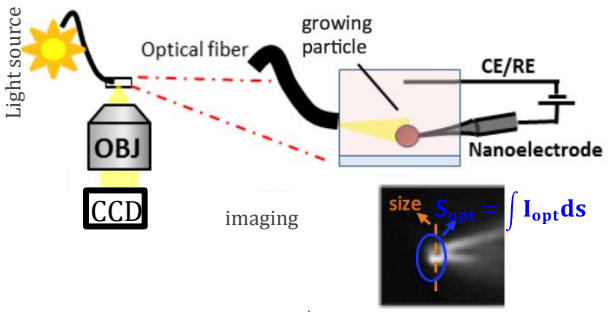

Figure 1. Experimental setup to monitor particle growth and electrochemistry. Images on CCD allow estimating: particle size from super-localization of pattern (along orange dotted line) formed at nanoelectrode, and particle light scattering intensity S_{opt} by averaging optical intensity I_{opt} over particle region (blue).

EXPERIMENTAL SECTION

Dark-field optical microscopy was used to monitor the electrochemical reactions on a single particle supported by the apex of a nanoelectrode. The description of the principle can be found in our previous report. [38] Briefly, a quartz capillary is axially pulled during laser-heating (laser puller, P-2000, Sutter instruments), giving rise to nanopipettes. Each nanopipette is subsequently filled with butane gas and heated in an inert atmosphere, triggering pyrolysis of the carbon precursor inside the nanopipette and generating a layer of conductive carbon on the internal glass walls that seals the nanopipette and forms a rigid carbon nanoelectrode.[15] The nanoelectrode is positioned in a droplet cell mounted on a thin glass slide (1 mm thickness) on top of an inverted microscope, mounted onto an air mattress anti-vibration stage, and equipped with a long working distance objective (x60, Numerical Aperture, NA=0.7). The nanoelectrode apex is illuminated under dark-field conditions (Fig.1) using a nearby multimode optical fiber (1mm core diameter, NA=0.2) coupled to a broadband high-intensity xenon arc lamp, and oriented perpendicularly to the objective axis. The incident illumination is not collected, but the light scattered by the nanoelectrode and particle is imaged on a camera (CCD) at a frequency of at least 2 images per second. As discussed below, two types of information were extracted from such wide-field optical images. First, edge super-localization allowed deducing the particle size. Second, the averaged scattered light, recorded locally at the ensemble formed by the nanoelectrode apex and the particle, S_{opt}, gave access to both the particle size and its chemistry.

Particle Sizing by Super-localization. Scattering essentially derives from refractive index discontinuities. Assuming a uniform and smooth object larger than the Point Spread Function (PSF) of the microscope, dark field illumination provides images of object edges, which can be described in a first approximation as the lateral spatial derivative of the refractive index. In addition, according to the Rayleigh criterion, the resolution of optical microscopy is reached when small objects are separated by a distance equal to the lateral radius of the PSF, usually defined as the distance between the center of the Airy disc and its first zero. Under non-coherent illumination, this resolution limit corresponds to $R_{PSF} \approx 1.22\lambda/2NA \approx 480nm$ for a central wavelength λ=550nm. The dark field image of a simple object can therefore be described as the convolution of the spatial derivative of the index with the PSF of the microscope (see Fig.2a).

A dark field image where two edges of a small object are too close ($d < R_{PSF}$) cannot be resolved, and attempts to quantify directly the object size through imaging below this limit is unfruitful. We discuss here strategies to overcome this limitation for the monitoring of the dynamic size variations of an object, depending on the relative values of its size and R_{PSF}.

Regime 1 – Particle Diameter Smaller than R_{PSF} ($2R_p<R_{PSF}$). Such nanoobjects cannot be resolved by optical microscopy, and their image cannot be reliably distinguished from the PSF of the microscope, regardless of their actual size (Fig.2a left). However, their scattering cross section is driven by the refractive indexes of the particle and its environment, and by the size of the particle, R_P. Sizing can therefore be directly obtained from the averaged intensity of the light scattering, S_{opt}, which is proportional to the scattering cross-section if the shape of the scattering pattern is stable (variations may induce changes in the efficiency of the collection by the objective). This cross-section can be related to particle size using either optical models (Mie theory)[35,37,40] or experimental cross-correlation by *ex situ* SEM analysis.[38,40]

A further strategy to estimate the size of particle below the diffraction limit exploits, as discussed in Supporting Information, SI, section S1, the full visible spectrum of the light scattering, S_{opt}. The spectrum of individual particle, obtained experimentally (Fig.S1, SI) by splitting the scattered light into two beam paths of equal intensity,[37d] is compared to Mie's theory allowing to further quantify CoOx particle size.

Regime 2 – Particle Diameter Comparable to R_{PSF} ($2R_p \sim R_{PSF}$). Once the particle diameter nears R_{PSF}, the edges of the particle behave as objects, which gradually become distinguishable according to the Rayleigh criterion (Fig.2a left). However, a broadening of the image of the particle compared to the PSF of the microscope can already be detected even for particles smaller than R_{PSF}. In principle, deconvolution by the PSF should lead to the actual size of the particle, but this is impractical considering experimental signal-to-noise ratios. In this case, the particle size variations are evaluated by fitting

the local scattering light intensity, I_{opt}, profile passing through the center of the particle by an individual Gaussian function. The Full Width at Half Maximum (FWHM) of this Gaussian is not an absolute measurement of particle size, but its variations can reliably be identified with variations in the size of the particle. This possibility is illustrated in Fig.2b for three successive images of the same particle during its growth, showing diffraction patterns of increasing width. In the profile associated to the third image, a shoulder near the center of the profile indicates that the particle edges start to be resolved, although the Rayleigh criterion is not fulfilled yet. This decreases the quality of the single Gaussian fit used to treat the experimental data as we approach regime 3. However, measuring the FWHM of the fitted Gaussian is shown to be a robust (error<10%) indicator of the particle growth.

Regime 3 - Particle Diameter Larger than PSF ($2R_p > R_{PSF}$). As discussed above, in this regime, the light-scattering edges of the particle can be resolved by dark field microscopy (Fig.2a right). A super-localization procedure can therefore be applied to estimate the position of the edges very precisely. An intensity profile, I_{opt}, along a diameter of the particle was fitted using two Gaussian functions. The position of each edge corresponds to the center of each function (its maximum as in Fig.2c), and the particle diameter corresponds to the distance between these edges. The accuracy of such scattering-based superlocalization is only limited by the signal-to-noise ratio of the image, and routinely reaches the 10nm-range.[43]

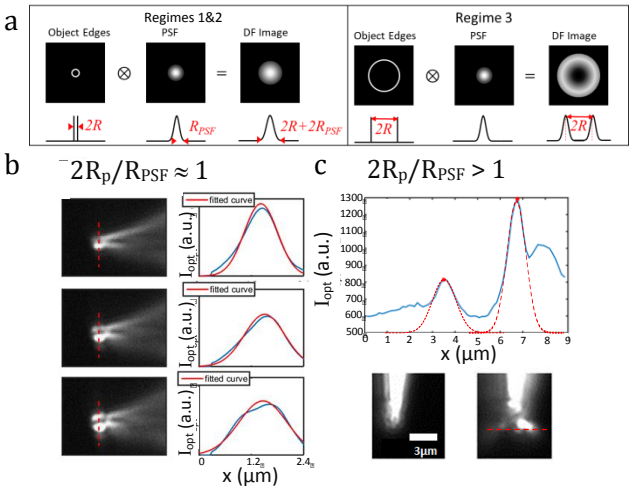

Figure 2. Super-localization sizing of particles. (a) Scheme of PSF convolution in optical imaging for resolution of the edges of an object (size: 2R). (b,c) Estimation of (b) size variation, (c) size of particles when they are (b) comparable or (c) much larger than the PSF: I_{opt} profiles (blue line, taken along red dashed lines in pictures) are fitted by Gaussian curves (red lines).

This discussion of three different regimes relies on strong assumptions regarding the particle geometry (smoothness and homogeneity) and the interpretation of the signals (direct proportionality between collected dark-field intensity and scattering cross section). However, as shown below, the continuity of the obtained measurements and the cross- comparison of various techniques are strong indications of their validity, and therefore of the applicability of the methods we propose here. A first validation is provided from ex situ SEM imaging of the electrodeposited particles, showing in Fig.S5a for examples 300nm and 2.9µm particles their general spherical shape. Noteworthy, harsh electrodeposition conditions (high current density) may produce particle overall spherical but presenting fractal features which can be imaged optically (Fig.S5b).

Considering the electrodeposition of spherical particles, we estimate that the growth of particles larger than 200-300nm in radius with sensitivity in radius ΔR_p between 10 and 50nm can be monitored using this method. Typically, for the deposition of Co-oxide onto a 300nm radius particle, this sensitivity corresponds roughly to the direct detection of an amount of deposited material, $\Delta n = 4\pi R_p^2 \Delta R_p V_m$, with V_m its molecular volume (typically >20cm^3/mol for cobalt oxides), which amounts to ca. 3amol (i.e. a sensitivity of ca. 2×10^6Co atoms).

Translating Optical Signal into Chemical Information. In addition to the electrochemical current and the particle size variation, the optical particle signature can be derived through the averaged intensity of scattered light intensity, S_{opt}. We have previously demonstrated that S_{opt} allows identifying the transformation of Co(0) into Co(II) species in particles ranging from 40 nm to 1 µm.[38] The optical signal, S_{opt}, then provides a direct estimate of the amount of optically addressable Co(II) material. Its redox transformation rate, or an equivalent optical current, i_{opt}, is readily obtained from the derivative of S_{opt} with respect to time according to:

$$i_{opt} = -\frac{dS_{opt}}{dt} \sim \frac{dn_{Co(III)}}{dt} = -\frac{dn_{Co(II)}}{dt} \qquad (1)$$

For visual comparison of i_{opt} and i_{EC}, the convention adopted in (1) is the same as that proposed for the reductive electrodeposition of Co by reduction of Co^{2+};[38] it yields a positive optical current for the transformation of Co(II) to Co(III) and therefore complements the anodic electrochemical current.

RESULTS AND DISCUSSION

Probing the Growth and Electrochromicity of Co-oxide Particles.

Fig.3 illustrates the optical monitoring of the growth of Co-oxide particles during potential cycling at a carbon nanoelectrode in a solution of Co^{2+}. In Fig.3a, a Co-oxide particle is grown from a Co nucleus preformed on a carbon nanoelectrode upon Co^{2+} reduction. It is detected at its earliest stage from the abrupt change in S_{opt}, (Reg.1 in Fig.3a, from A and approx. until 50s later), then its size variation is estimated when it is comparable to the PSF (Reg.2, regions B-C) or of micrometric dimension (Reg.3, region D). In Fig.3b, a 2µm particle is sized (Reg.3). In both figures, the particle apparent size (FWHM or R_p) is increasing while the nanoelectrode is polarized between potentials of 0.6–1Vvs Ag/AgCl. This on/off switching associated with the reversible transformation between Co(II) and Co(III) within the electrodeposited particle agrees with the higher absorption of the higher Co oxidation states, explaining the known electrochromicity of metal oxides such as iron[44] or cobalt oxides. These observations are in close agreement with results reported for thin films[10] or single dried $LiCoO_2$ nanosheets,[34] where respectively increased UV-vis light absorption or decreased SPR signals were detected during Co(II)/Co(III) oxidation.

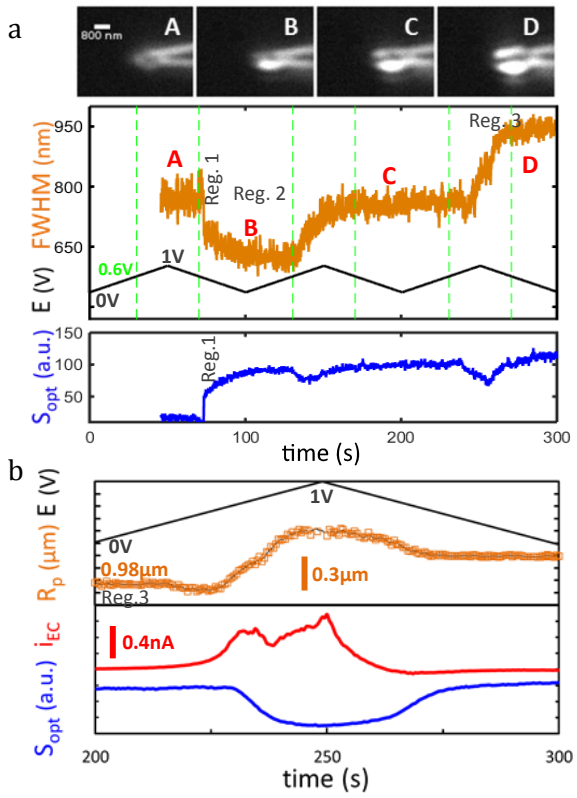

Figure 3. Growth of (a) diffraction limited or (b) micrometric Co-oxide particles from carbon nanoelectrodes monitored by dark-field microscopy during anodic cycles (black lines) at 20 mV/s in 4 mM $CoCl_2$ + 0.05 M KCl. (a) red line indicates time when the particle is detected, later it becomes resolvable (Reg.2, size comparable to PSF, here 650nm). The particle size variation is extracted from the variation in the FWHM (see Fig. 2b); vertical green guidelines correspond to E = 0.6 V. (b) edges of the particle (see Fig. 2c, Reg.3) are resolved, and particle size, R_p is estimated, along with S_{opt} and i_{EC} during a cycle.

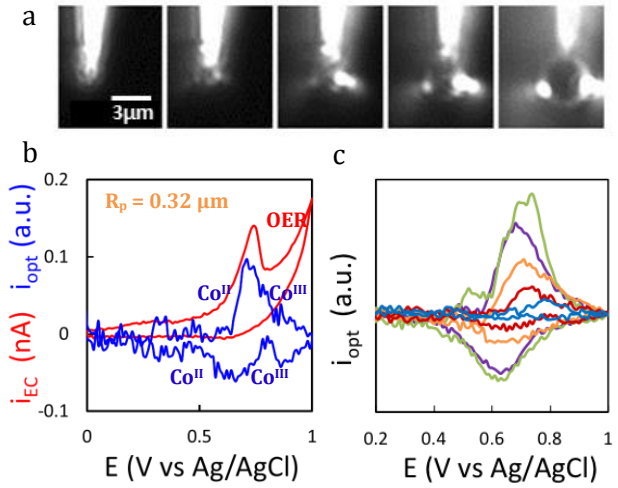

Figure 4. Particle growth and optical response during repetitive anodic cycles. (a) optical images. (b) Derivation of direct electrochemical data from the optical response of the particle (opCV) and comparison to conventional eCV. (c) Comparison of opCVs at different stages of particle growth. Particle radii (in µm) are in images (a) and opCVs (d) 0.3 (blue), 0.36 (orange), 0.70 (yellow), 0.98 (purple) and 1.36 (green).

According to equation (1), an opto-voltammogram (opCV), i_{opt}-E, is derived characterizing this electrochromicity and complementing the electrochemical voltammogram, eCV. Fig.4b shows and example of opCV and eCV recorded at nanoelectrodes cycled in a Co^{2+} solution between 0 and 1V during the successive anodic electrodepositions of Co-oxide onto a single particle. The different opCVs and eCVs recorded for the successive cycles are given respectively in Figs.4c and S6 (pictures of the particle in Fig.4a). The opCVs in Figs.4b,c show a bell-shaped curve characteristic of the reaction of a surface-confined species. Both the opCVs and eCVs presented in Figs.4b and S4 (SI) show remarkably similar features with a forward anodic peak located at E_p =0.68V (80–100mV half-width). It suggests that both voltammograms have a common underlying basis, the Co(II)/Co(III) transformation, generally described as: [2-4,7]

$$Co^{II}(OH)_2 \rightarrow Co^{III}OOH + e^- + H^+ \quad (2)$$

or

$$Co^{II}(OH)_2 + H_2O \rightarrow Co^{III}(OH)_3 + e^- + H^+ \quad (2')$$

While in the eCV the tail of the current signals for the Co(II) to Co (III) transition are convoluted with the onset of current for the OER, the opCV shows only peaks for the change of Co redox state (Fig.4b). Additionally, the reversibility of the Co(II)/Co(III) transformation is more clearly detected in the opCV from the reverse cathodic peak detected at E_p = 0.63V (Fig.4b,c). Its absence from the eCV may be related to the participation of the Co(III) species into catalytic reaction such as water splitting.

Thus, the opCVs provide complementary insight for electrochemical reactions of the active species, particularly when those signals are hidden in conventional CV. We then use these complementary optical and size information obtained *in situ* to depict mechanistic aspects of single Co-oxide particle electrochemistry.

Electrochemical Breathing of Co-oxide Particles. The electrochemistry of a Co-oxide particle was first addressed in KCl electrolyte in the absence of Co^{2+} ions. Fig.5 provides the time evolution, during a voltammogram, of i_{EC}, i_{opt} and R_p for a 0.6µm radius particle. As the particle is oxidized, and concomitantly optically switched off, its size also increases by 8%. Upon potential reversal the particle returns back to its original size, but much more slowly. This breathing corresponds to a ca. 25% volume expansion/shrinking during the potential cycle. The instantaneous volume variation $dV_p(t)/V_p^{(t=0)}dt = 4\pi R_p^2 dR_p/V_p^{(t=0)}dt$, normalized to the initial particle volume denoted $V_p^{(t=0)}$, is plotted in the lower panel of Fig.5. It correlates well with i_{opt} (or i_{EC}), suggesting that the volume expansion is also related to the Co(II)/Co(III) charge transfer process (2 or 2').

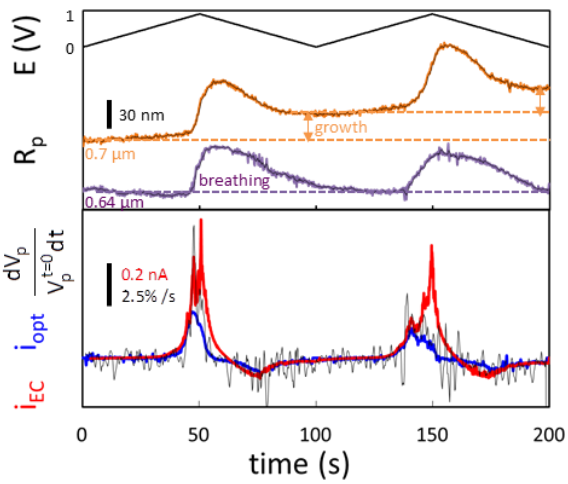

Figure 5. Particle size and optical response during anodic cyclic votammetry performed in a solution of 0.05 M KCl in the absence (purple, red, blue, black lines) or presence (orange line, opCV and eCV given in Fig.S7 in SI) of 4 mM Co^{2+} ions. A reversible volume change (breathing) of the particle is detected during the particle oxidation. The normalized dynamic volume change (black line) correlates with both opCV and eCV.

The correlation between both i_{EC} or i_{opt} and dV_p/dt can be rationalized by Faradaic analysis according to (3), or mass conservation and (1) according to (3'):

$$dV_p/dt = i_{EC}\,\Delta V_m/F \qquad (3)$$

$$dV_p/dt = \Delta V_m\, dn_{Co(III)}/dt \approx \Delta V_m\, i_{opt} \qquad (3')$$

where ΔV_m corresponds to the change in molar volume during the Co(II)/Co(III) transformation.

The instantaneous volume expansion can reach up to 10% per s. The fast expansion and slower shrinking of the particle are also related to its faster oxidation and slower backward reduction (more clearly detected on the backward i_{opt} signal). It suggests that the Co(II)/Co(III) transformation is accompanied by a limiting process such as phase transformation and/or insertion/deinsertion, which is in favour of reaction (2') where water (or anion) is inserted in the particle to accommodate the change in particle polarization or change between a compact $Co(OH)_2$ structure (V_m=25.8cm^3/mol[45a]) and a less compact $Co(OH)_3$ structure (V_m=36.8 cm^3/mol[45b], yielding ΔV_m=11 cm^3/mol). For the 0.64µm radius particle depicted in Fig.5, the peak in dV_p/dt is about $0.025V_p^{(t=0)}$, which is 0.028µm^3/s. The Faraday law is difficult to estimate accurately as the Co(II) oxidation is convoluted with the OER. However, from the estimate of the electrochemical current at the peak potential, i_p~0.2nA in Fig.5, an estimate of the instantaneous change in molar volume of the material is obtained from (3). Its value $\Delta V_m = F dV_p/i_p dt$ = 13cm^3/mol is in good agreement with the value expected for the Co(II)/Co(III) hydroxide transformation. Such large deformation evidenced at the single particle level may also explain why the anodic electrodeposition of Co-oxides generates particle arrays rather than homogeneous films. Moreover, the chemical transformation and deformation detected may be difficult to probe *ex situ*, owing to the fast chemical reconstruction of Co-hydroxides in air.

Cobalt-oxide Electrodeposition. Next the electrochemistry of the particle was addressed while Co^{2+} ions are present in the electrolytic solution. As observed in Figs.3b and 5 (orange line), in addition to the reversible particle breathing, the particle is larger at the end of the potential cycle than at its beginning. This means that the pure electrochemical transformation of the particle (and its breathing) occurs concomitantly to the anodic deposition of more cobalt material on it (particle growth). This anodic electrodeposition of Co-oxide material is also confirmed by (i) the enlargement of the particle observed in pictures (Fig.4a) of the particle obtained at the end of each repetitive potential cycle and, (ii) the dynamic super-resolved R_p variations during these cycles (Fig.S7, SI). The electroprecipitation (4) of Co(III) material from the direct oxidation of Co^{2+} ions at the particle surface is suggested based on the poor solubility of Co^{3+} ions:[45c]

$$Co^{2+} + 3H_2O \rightarrow Co^{III}(OH)_3 + e^- + 3H^+ \qquad (4)$$

As both particle breathing (2') and electroprecipitation (4) occur concomitantly, a dynamic Faradaic analysis during the voltammograms is quite speculative. However, a global analysis was performed by comparing the overall charge exchanged and particle size variation between the end and beginning of each voltammogram. This gives a molar volume of the deposited material of V_m=30±2cm^3/mol, suggesting that during the overall CV (back and forth) a $Co(OH)_2$-like material is electroprecipitated through a global 1 e^- transfer process.

Electrocatalysis of the OER

Combined optical and electrochemical signatures of the particles allows depicting their electrocatalytic properties toward water splitting. Figures 6a and 6b describe the catalysis of water splitting reaction at both the level of the Co(III)/Co(IV) and Co(II)/Co(III) transitions, respectively.

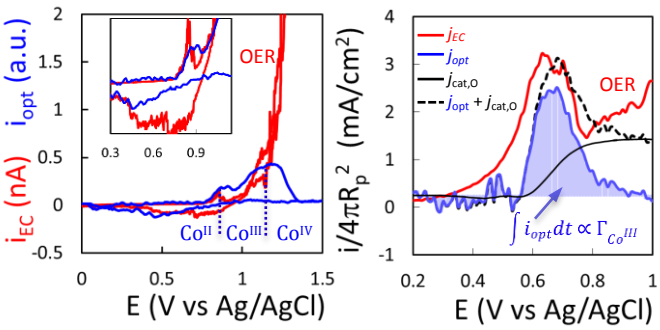

Figure 6. Catalysis of the OER by (a) Co(IV) or (b) Co(III) species. (a) a R_p=0.83µm particle is submitted to more anodic potential: both Co(II)/Co(III) and Co(III)/Co(IV) transformation are detected on the opCV (dashed blue lines) and eCV (with OER catalysis inferred for the large i_{EC} increase). (b) Comparison of the forward scan of the surface-normalized opCV and eCV for evaluation of catalysis of the OER by Co(III) on R_p^{init}=0.98µm particle. Integration of the opCV current density, j_{opt}, yields the E-evolution of Co(III) species in the particle, $\Gamma_{Co(III)}$, from which OER catalysis contribution, $j_{cat.O}$, is obtained. Dashed lines: sum of both contributions. Other particles in Fig. S6" (SI).

Electrocatalysis of the OER by Co(III)/Co(IV) Species. If the potential is scanned to higher anodic potential (Fig.6a), a second peak is detected in the opCV, which is ascribed to the

transition of Co(III) to Co(IV). The electrocatalytic properties of Co material towards water oxidation was rationalized by mechanisms[4] suggesting, based on the analysis of CV features, that a complex electron-proton-coupled transfer occurs, implying Co(II), Co(III) and Co(IV) dinuclear species:

$$HOOCo^{III}Co^{III}OOH \rightarrow OCo^{IV}Co^{IV}O + 2H^+ + 2e^- \quad (5)$$

$$O_2Co^{IV}Co^{IV}O_2 + 2\,H_2O \rightarrow H_2O_2Co^{II}\,Co^{II}O_2H_2 + O_2 \quad (5')$$

At the potential of the OER catalysis, the Co(III) dinuclear species is readily oxidized in two successive 1-electron transfer processes then generating the $Co^{IV}Co^{IV}$ species (5). The latter is involved in the oxidation of water (5') regenerating, in a redox catalysis fashion, the Co(II) dinuclear species automatically converted into the Co(III) dinuclear at the potential of OER catalysis. By further increasing the potential of the anodic scan, beyond the Co(II)/Co(III) transition, as shown in Figs.6a and S8 (SI) we access such catalysis. In Fig.6a, the particle was not fully extinguished at the first Co(II)/Co(III) stage and a second optical peak, ca. 3 times more intense, was observed in the opCV at 0.3V more anodic potentials than the Co(II)/Co(III) stage, indicating that the Co(III)/Co(IV) transformation can also be monitored optically. Besides, the electrochemical current at this second oxidation stage is about 10 times larger than at the first stage suggesting that a much higher amount of electrons is involved, in agreement with efficient catalysis of the OER through (5+5').

When the particle scattering is fully extinguished at the first Co(II)/Co(III) stage, as in Fig.S8 (SI), the second oxidation stage is at optical noise level and cannot be detected in the opCV. However, the catalysis reaction is detected in the eCV by a steady-state wave with an $E_{1/2}$, which is, in Fig.6a, 0.28 V more positive than the Co(II)/Co(III) process revealed by the opCV. This confirms again that the electrocatalysis may be quantified by the complementary signals.

Catalysis by Co(II)/Co(III) Species. Co(III) species are also assumed to catalyze the OER, however at a much lower extent than Co(IV).[46] The comparison of opCV and eCV in Fig.4b shows a reversible optical feature while the backward electrochemical signature is much less reversible. Indeed, while the opCV directly addresses the reversible Co(II)/Co(III) transformation during the potential cycle, the lack of reversibility of the eCV is in agreement with a catalytic regeneration of Co(II) species, for example in the catalytic cycle:

$$H_2O_2Co^{II}Co^{II}O_2H_2 \rightarrow HOOCo^{III}Co^{III}OOH + 2e + 2H^+ \quad (6)$$

$$HOOCo^{III}Co^{III}OOH + H_2O \rightarrow H_2O_2Co^{II}Co^{II}O_2H_2 + ½O_2 \quad (6')$$

A quantitative analysis of this catalytic cycle was obtained from the complementary inspection of the opCV.

the number of electrons exchanged over the whole process (particle oxidation and electrocatalytic water splitting) is extracted from the eCV. In order to account for particle expansion (breathing and electrodeposition), which is inherent to the particle electrochemistry, the currents (electrochemical and optical) are converted into current densities, $i_{EC}/4\pi R_p^2$ and $i_{opt}/4\pi R_p^2$, provided through the instantaneous particle optical sizing. For the range of particle sizes described in Fig. 4a, all current density features (Fig.S6', SI) overlap reasonably suggesting that the electrochemical and optical activities of the particle are determined by a surface process.

In this respect the optical and electrochemical current densities for the four particles, of size ranging from 0.6 to 3 µm, successively grown on the same nanoelectrode are compared in Fig.6b and S6" (SI). A closer examination of those curves, as in Figs.6 and S6" (SI), show several common features for all particle sizes, described here in order of occurrence from lowest to highest potential: (i) at 0.56V the eCV shows a shoulder in i_{EC} before the onset of the opCV current; (ii) both the optical and electrochemical peaks are rather large (160±10 mV for the FWHM peaks while Nernstian bell-shaped voltammograms for surface processes are described by 96mV FWHM) and, (iii) while i_{opt} returns to zero (for E>0.8V) i_{EC} levels at a steady-state but non-null value. All these features can be rationalized with respect to previous studies. (i) The initial EC current shoulder can be attributed to a capacitive contribution associated to the doping of the semiconducting Co-oxide material.[4] (ii) The large EC and optical peaks is consistent with previous observation of either two electrochemical contributions assigned from a spectroscopic peak-splitting[10] or a broad EC peak related to the intervention of a broad distribution of different CoOx structures.[4] (iii) Finally, the zero-optical current value indicates that while the Co(II) material has been converted into Co(III), constant regeneration of Co(II) species in a redox catalytic fashion explains the steady-state electrochemical current value. This is indicative of a redox catalysis loop, as depicted in (6+6') where the Co(III) species is involved in the oxidation of H_2O by regeneration of the initial Co(II).

A quantitative analysis of these different aspects is proposed in Figs.6b and S6" (SI) by assuming that the optical current density, j_{opt}, is proportional to the derivative of the surface concentration of the Co(III) species $\Gamma_{Co(III),O}$ (without calibration in a.u./cm^2):

$$j_{opt} \propto \frac{d\Gamma_{Co(III),O}}{dt} \quad (7)$$

Therefore the catalytic contribution of the current density, j_{cat}, associated to the regeneration of Co(II) species through (6') with apparent water splitting rate k_{cat} (in s^{-1}) is expected to follow:

$$j_{cat,O} = k_{cat}\Gamma_{Co(III),O} \propto k_{cat}\int j_{opt}\,dt \quad (8)$$

This catalytic contribution, estimated from the integration of the optical current (i.e. the filled area of the opCV in Fig.6b), is represented as the sigmoidal-like black line in Fig.6b and S6". The sum of both contributions, $j_{opt}+j_{cat,O}$, given as the dashed black line in Fig.6b and S6", overlaps reasonably with the electrochemical current in the eCV (red line) for all four particles. This overlap is obtained with the same scaling parameter of i_{opt} and a catalytic reaction rate k_{cat} =0.12±0.06s^{-1}. This value, considerably lower than those observed for the water splitting reaction by Co(IV) species, is actually in agreement with that estimated from the interrogation mode of scanning electrochemical microscopy (SECM) of thin Co(III) oxide layers.[46]

CONCLUSION

The concept of super-localization allowed monitoring size variation of individual particles with up to 10nm precision. The strategy was used during the dark-field optical imaging of single particles of sizes from the diffraction limit to a few micrometers (here from 0.6 to 3µm). Such light-scattering

optical microscopy technique is generally used to gain chemical information carried by the intensity of light scattered by an individual particle (here change in redox state). The super-localization proposed herein complements the technique by an indirect estimate of the particle size variation. This is demonstrated for the *in operando* monitoring of the oxidation and electrodeposition of single cobalt-oxide particles grown on a nanoelectrode scaffold. The light scattered by the particle is switched off and on reversibly during the Co(II)-Co(III) conversion, as a result of the stronger light absorption by cobalt oxides with higher oxidation states (and electrochromicity of metal oxides). The indirect dynamic estimate of the particle size shows that the Co(II)-Co(III) oxidation of cobalt-oxide particle is accompanied by ~20% volume change. The same particle breathing is observed during particle growth (when a Co^{2+} solution is oxidized), which is also quantified. It is suggested that the oxidation of Co^{2+} solution most likely produces cobalt-hydroxide material. The strong volume expansion (breathing) is then attributed either to the change in cobalt-hydroxide molar volume, or insertion of water or ionic material upon charge transfer. This reversible volume variation is faster during the anodic than during the cathodic exploration, which may be a limiting aspect of the use of such materials for fast energy storage devices. Finally, the complementarity of size, optical and electrochemical signature allowed characterizing the electrocatalytic properties of such materials. While Co(IV) species can be identified both optically and from strong catalysis of the OER, the comparison of the optical and electrochemical voltammograms of the Co(II)/Co(III) system allows quantifying the catalytic strength of Co(III) species.

This work further highlights the benefits of correlated optical microscopy and electrochemistry for single particle studies. The super-localization approach demonstrated here for the investigation of materials relevant to electrochemical energy conversion, may also apply to a wide range of materials for energy storage or presenting stimuli-responsive deformation.

ASSOCIATED CONTENT

Supporting Information

The Supporting Information is available free of charge on the ACS Publications website.

Size from spectroscopy. Voltammograms and R_p for the different cycles in Fig.4c. Normalization by particle surface area. Deconvolution by different current contributions for other eCV and opCV of growing particles in Fig. 5. OER catalysis. (PDF)

AUTHOR INFORMATION

Corresponding Author

* frederic.kanoufi@univ-paris-diderot.fr

ACKNOWLEDGMENT

VB thanks DAAD for funding of his stay at Bochum. FK is grateful for financial support by the Agence Nationale pour la Recherche (NEOCASTIP ANR-15-CE09-0015-02 project). JC and WS are grateful for financial support by the Deutsche Forschungsgemeinschaft in the framework of the cluster of excellence Resolv (EXC1069) and the BMBF (NEMEZU project 03SF0497B).

REFERENCES

(1)X. Deng, H. Tüysüz, *ACS Catal.* Cobalt-Oxide-Based Materials as Water Oxidation Catalyst: Recent Progress and Challenges **2014**, *4*, 3701-3714.

(2)Kanan, M. W.; Nocera, D. G. In situ formation of an oxygen-evolving catalyst in neutral water containing phosphate and Co^{2+}. *Science* **2008**, *321*,1072-1075.

(3) Bediako, D. K.; Costentin, C.; Jones, E. C.; Nocera, D. G.; Savéant, J.-M. Proton-Electron Transport and Transfer in Electrocatalytic Films. Application to a Cobalt-Based O-2-Evolution Catalyst. *J. Am. Chem. Soc.* **2013**, *135*, 10492-10502.

(4)Costentin, C.; Porter, T. R.; Savéant, J.-M. Conduction and Reactivity in Heterogeneous-Molecular Catalysis: New Insights in Water Oxidation Catalysis by Phosphate Cobalt Oxide Films. *J. Am. Chem. Soc.* **2016**, *138*, 5615-5622.

(5)Subbaranam, R.; Tripkovic, D.; Chang, K.-C.; Strmcnik, D.; Paulikas, A. P.; Hirunsit, P.; Chan, M.; Greeley, J.; Stamenkovic, V.; Markovic, N. M. Trends in activity for the water electrolyser reactions on 3d M(Ni,Co,Fe,Mn) hydr(oxy)oxide catalysts. *Nat. Mater.* **2012**, *11*, 550-557.

(6)Walton, A.S.; Fester, J.; Bajdich, M.; Arman, M. A.; Osiecki, J.; Knudsen, J.; Vojvodic, A.; Lauritsen, J. V. Interface Controlled Oxidation States in Layered Cobalt Oxide Nanoislands on Gold. *ACS Nano* **2015**, *9*, 2445-2453.

(7)Surendranath, Y.; Lutterman, D. A.; Liu, Y.; Nocera, D. G. Nucleation, Growth, and Repair of a Cobalt-Based Oxygen Evolving Catalyst. *J. Am. Chem. Soc.* **2012**, *134*, 6326-6336.

(8)Reikowski, F.; Maroun, F.; Di, N.; Allongue, P.; Ruge, M.; Stettner, J.; Magnussen, O. M. In situ surface X-ray diffraction study of ultrathin epitaxial Co films on Au(111) in alkaline solution. *Electrochim. Acta* **2016**, *197*, 273-281.

(9)Farrow, C. L.; Bediako, D. K.; Surendranath, Y.; Nocera, D. G.; Billinge, S. J. L. Intermediate-Range Structure of Self-Assembled Cobalt-Based Oxygen-Evolving Catalyst. *J. Am. Chem. Soc.* **2013**, *135*, 6403-6406.

(10)Risch, M.; Ringleb, F.; Kohlhoff, M.; Bogdanoff, P.; Chernev, P.; Zaharieva, I.; Dau, H. Water oxidation by amorphous cobalt-based oxides: in situ tracking of redox transitions and mode of catalysis. *Energy Environ. Sci.* **2015**, *8*, 661-674.

(11)Surendranath, Y.; Dinca, M.; Nocera, D. G. *J.* Electrolyte-Dependent Electrosynthesis and Activity of Cobalt-Based Water Oxidation Catalysts. *Am. Chem. Soc.* **2009**, *131*, 2615-2620.

(12)Liu, Y.; Nocera, D. G. Spectroscopic Studies of Nanoparticulate Thin Films of a Cobalt-Based Oxygen Evolution Catalyst. *J. Phys. Chem. C* **2014**, *118*, 17060-17066.

(13)Floate, S.; Hyde, M.; Compton, R. G. Electrochemical and AFM studies of the electrodeposition of cobalt on glassy carbon: an analysis of the effect of ultrasound. *J. Electroanal. Chem.* **2002**, *523*, 49-63.

(14)Burke, M. S.; Enman, L. J.; Batchellor, A. S.; Zou, S.; Boettcher, S. W. Oxygen Evolution Reaction Electrocatalysis on Transition Metal Oxides and (Oxy)hydroxides: Activity Trends and Design Principles. *Chem. Mater.* **2015**, *27*, 7549-7558.

(15)Clausmeyer, J.; Masa, J.; Ventosa, E.; Öhl, D.; Schuhmann, W. Nanoelectrodes reveal the electrochemistry of single nickelhydroxide nanoparticles. *Chem. Commun.* **2016**, *52*, 2408-2411.

(16)Bartling S. C., Yin, S.Vajda. et al. Pronounced Size Dependence in Structure and Morphology of Gas-Phase Produced, Partially Oxidized Cobalt Nanoparticles under Catalytic Reaction Conditions. *ACS Nano* **2015**, *9*, 5984-5998.

(17)Mirkin, M. V.; Sun, T.; Yu, Y.; Zhou, M. Electrochemistry at One Nanoparticle. *Acc. Chem. Res.* **2016**, *49*, 2328-2335.

(18)Kim, J.; Dick, J.E.; Bard, A. J. Advanced Electrochemistry of Individual Metal Clusters Electrodeposited Atom by Atom to Nanometer by Nanometer. *Acc. Chem. Res.* **2016**, *49*, 2587-2595.

(19)Anderson T. J.; Zhang, B. Single-Nanoparticle Electrochemistry through Immobilization and Collision. *Acc. Chem. Res.* **2016**, *49*, 2625-2631.

(20)Clausmeyer, J.; Schuhmann, W. Nanoelectrodes: Applications in electrocatalysis, single-cell analysis and high-resolution electrochemical imaging. *Trend. Anal. Chem.* **2016**, *79*, 46-59.

(21) Xiao, X.; Bard A. J. Observing single nanoparticle collisions at an ultramicroelectrode by electrocatalytic amplification. *J. Am. Chem. Soc.* **2007**, *129*, 9610-9612.

(22)Ebejer, N.; Güell, A. G.; Lai, S. C. S.; McKelvey, K.; Sowden, M. E.; Unwin, P. R. Scanning Electrochemical Cell Microscopy: A Versatile Technique for Nanoscale Electrochemistry and Functional Imaging. *Annu. Rev. Anal. Chem.* **2013**, *6*, 329-351.

(23)Kang, M.; Perry, D.; Kim Y. R.; Colburn A. W.; Lazenbt, R. A.; Unwin P. R. Time-Resolved Detection and Analysis of Single Nanoparticle Electrocatalytic Impacts. *J. Am. Chem. Soc.* **2015**, *137*, 10902–10905.

(24)Yu, Y.; Gao, Y.; Hu, K.; Blanchard, P. Y.; Noël, J.-M.; Nareshkumar, T.; Phanie, K. L.; Griedman, G.; Gogotsi, Y.; Mirkin, M. V. Electrochemistry and Electrocatalysis at Single Gold Nanoparticles Attached to Carbon Nanoelectrodes. *ChemElectroChem* **2015**, *2*, 58-63.

(25)Clausmeyer, J.; Botz, A.; Öhl, D.; Schuhmann. W. The oxygen reduction reaction at the three-phase boundary: nanoelectrodes modified with Ag nanoclusters. *Faraday Discuss.* **2016**,*193*, 241-250.

(26) Li, Y.; Cox, J. T.; Zhang, B. Electrochemical Responses and Electrocatalysis at Single Au Nanoparticles. *J. Am. Chem. Soc.* **2010**, *132*, 3047-3054.

(27)Kim, J.; Bard, A. J. Electrodeposition of Single Nanometer-Size Pt Nanoparticles at a Tunneling Ultramicroelectrode and Determination of Fast Heterogeneous Kinetics for $Ru(NH_3)(_6)(^{3+})$ Reduction. *J. Am. Chem. Soc.* **2016**, *138*, 975-979.

(28)Sun, T.; Yu, Y.; Zacher, B. J.; Mirkin, M. V. Scanning Electrochemical Microscopy of Individual Catalytic Nanoparticles. *Angew. Chem. Int. Ed.* **2014**, *53*, 14120-14123.

(29) Actis, P.; Tokar, S.; Clausmeyer, J.; Babakinejad, B.; Mikhaleva, S.; Cornut, R.; Takahashi, Y.; López Córdoba, A.; Novak, P.; Shevchuck, A. I.; Dougan, J. A.; Kazarian, S. G.; Gorelkin, P. V.; Erofeev, A. S.; Yaminsky, I. V.; Unwin, P. R.; Schuhmann, W.; Klenerman, D.; Rusakov, D. A.; Sviderskaya, E. V.; Korchev, Y. E. Electrochemical Nanoprobes for Single-Cell Analysis. *ACS Nano* **2014**, *8*, 875-884.

(30)Takahashi, Y.; Shevchuk, A. I.; Novak, P.; Zhang, Y.; Ebejer, N.; Macpherson, J. V.; Unwin, P.R.; Pollard, A. J.; Roy, D.; Clifford, C. A.; Shiku, H.; Matsue, T.; Klenerman, D.; Korchev, Y. E. Multifunctional Nanoprobes for Nanoscale Chemical Imaging and Localized Chemical Delivery at Surfaces and Interfaces. *Angew. Chem. Int. Ed.* **2011**, *50*, 9638 –9642.

(31)Hemonnot, C. Y. J.; Ranke, C.; Saldanha, O.; Graceffa, R.; Hagemann, J.; Köster, S. Following DNA Compaction During the Cell Cycle by X-ray Nanodiffraction. *ACS Nano* **2016**, *10*, 10661-10670.

(32)Hrauda, N.; Zhang, J.; Wintersberger, E.; Etzelstorfer, T.; Mandl, B.; Stangl, J.; Carbone, D.; Holy, V.; Jovanovic, V.; Biasotto, C.; Nanver, L. K.; Moers, J.; Grützmacher, D.; Bauer, G. X-ray Nanodiffraction on a Single SiGe Quantum Dot inside a Functioning Field-Effect Transistor. *Nano Lett.* **2011**, *11*, 2875-2880.

(33)Hodnik, N.; Dehm, G.; Mayrhofer, K. J. J. Importance and Challenges of Electrochemical in Situ Liquid Cell Electron Microscopy for Energy Conversion Research. *Acc. Chem. Res.* **2016**, *49*, 2015-2022.

(34)a. Jiang, D.; Jiang, Y.; Li, Z.; Liu, T.; Wo, X.; Fang, Y.; Tao, N.; Wang, W.; Chen, H.-Y. Optical Imaging of Phase Transition and Li-Ion Diffusion Kinetics of Single $LiCoO_2$ Nanoparticles During Electrochemical Cycling. *J. Am. Chem. Soc.* **2017**, *139*, 186-192; b. Sun, L.; Jiang, D.; Li, M.; Liu, T.; Yuan, L.; Wang, W.; Chen, H.-Y. Collision and Oxidation of Single LiCoO2 Nanoparticles Studied by Correlated Optical Imaging and Electrochemical Recording. *Anal. Chem.* **2017**, *89*, 6051-6055.

(35)a. Fang, Y.; Wang, W.; Wo, X.; Luo, Y.; Yin, S.; Wang, Y.; Shan, X.; Tao, N. Plasmonic Imaging of Electrochemical Oxidation of Single Nanoparticles. *J. Am. Chem. Soc.* **2014**, *136*, 12584-12587; b. Fang, Y.; Wang, H.; Yu, H.; Liu, X.; Wang, W.; Chen, H.-Y.; Tao, N. J. Plasmonic Imaging of Electrochemical Reactions of Single Nanoparticles. *Acc. Chem. Res.* 2016, *49*, 2614-2624; c. Yuan, T.; Wang, W. Studying the electrochemistry of single nanoparticles with surface plasmon resonance microscopy. *Curr. Op. Electrochem.* **2017**, *1*, 17-22.

(36)Fosdick, S. E.; Anderson, M. J.; Nettleton, E. G.; Crooks, R. M. Correlated Electrochemical and Optical Tracking of Discrete Collision Events. *J. Am. Chem. Soc.* **2013**, *135*, 5994-5997.

(37)a. Brasiliense, V.; Patel, A. N.; Martinez-Marrades, A.; Shi, J.; Chen, Y.; Combellas, C.; Tessier, G.; Kanoufi, F. Correlated Electrochemical and Optical Detection Reveals the Chemical Reactivity of Individual Silver Nanoparticles. *J. Am. Chem. Soc.* **2016**, *138*, 3478–3483; b. Patel, A. N.; Martinez-Marrades, A.; Brasiliense, V.; Koshelev, D.; Besbes, M.; Kuszelewicz, R.; Combellas, C.; Tessier, G.; Kanoufi, F. Deciphering the Elementary Steps of Transport-Reaction Processes at Individual Ag Nanoparticles by 3D Super localization Microscopy. *Nano Lett.* **2015**, *15*, 6454–6463; c. Brasiliense, V.; Berto, P.; Combellas, C.; Tessier, G.; Kanoufi, F. Electrochemistry of Single Nanodomains Revealed by Three-Dimensional Holographic Microscopy. *Acc. Chem. Res.* **2016**, *49*, 2049-2057; d. Brasiliense, V.; Berto, P.; Combellas, C.; Kuszelewicz, R.; Tessier, G.; Kanoufi, F. Electrochemical transformation of individual nanoparticles revealed by coupling microscopy and spectroscopy. *Faraday Discuss.* **2016**, *193*, 339-352.

(38)Brasiliense, V.; Clausmeyer, J.; Dauphin, A.L.; Noël, J.-M.; Berto, P.; Tessier, G.; Schuhmann, W.; Kanoufi, F. Optoelectrochemical In Situ Monitoring of the Cathodic Formation of Single Cobalt Nanoparticles. *Angew. Chem. Int. Ed.* **2017**, *56*, 10598-10601.

(39)Byers, C. P.; Hoener, B. S.; Chang, W.-S.; Link, S.; Landes, C. F. Single-Particle Plasmon Voltammetry (spPV) for Detecting Anion Adsorption. *Nano Lett.* **2016**, *16*, 2314-2321.

(40)Hill, C. M.; Pan, S. A Dark-Field Scattering Spectroelectrochemical Technique for Tracking the Electrodeposition of Single Silver Nanoparticles. *J. Am. Chem. Soc.* **2013**, *135*, 17250-17253.

(41)Hao, R.; Fan, Y.; Zhang, B. Imaging Dynamic Collision and Oxidation of Single Silver Nanoparticles at the Electrode/Solution Interface. *J. Am. Chem. Soc.* **2017**, *139*, 12274–12282.

(42)Hyde, M. E.; Compton, R. G. A review of the analysis of multiple nucleation with diffusion controlled growth. *J. Electroanal. Chem.* **2003**, *549*, 1-12.

(43)Martinez-Marrades, A.; Rupprecht, J.-F.; Gross, M.; Tessier, G. Stochastic 3D optical mapping by holographic localization of Brownian scatterers. *Opt. Express* **2014**, *22*, 29191-29203.

(44)Chakri, S.; Patel, A.N.; Frateur, I.; Kanoufi, F.; Sutter, E.M.M.; Tran, T.T.M.; Tribollet, B.; Vivier, V. Imaging of a Thin Oxide Film Formation from the Combination of Surface Reflectivity and Electrochemical Methods. *Anal. Chem.* **2017**, *89*, 5303-5310.

(45)a. Perry, D.L. *Handbook of inorganic compounds*, 2nd ed.; CRC Press: Boca Raton, 2011; p132; b. ibid, for $Co(OH)_3$,$3H_2O$, p137; c. The solubility product[d] of $Co(OH)_3$, K_s=1.6 10^{-44} M^4, suggests that Co^{3+} ions readily precipitate into Co(III) hydroxide material for any pH > 0.2; d. Olmsted, J.; Williams, G. M. *Chemistry: the molecular science*, 2nd Ed.; Wm. C. Brown: Dubuque, 1997; p A34.

(46)Ahn, H. S.; Bard, A. J. Surface Interrogation of CoPi Water Oxidation Catalyst by Scanning Electrochemical Microscopy. *J. Am. Chem. Soc*. **2015**, *137*, 612-615.

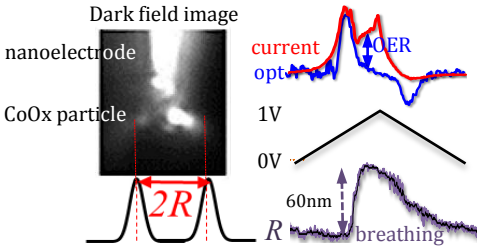
Dark field image
nanoelectrode
CoOx particle
2R
current
opt
OER
1V
0V
60nm
R
breathing